Chemical Engineering Journal 331 (2018) 492–500

Contents lists available at ScienceDirect

Chemical Engineering Journal

journal homepage: www.elsevier.com/locate/cej

Arsenic adsorption on α-MnO_2 nanofibers and the significance of (1 0 0) facet as compared with (1 1 0)

Jinming Luo[a,b,c], Xiaoyang Meng[c], John Crittenden[c], Jiuhui Qu[a], Chengzhi Hu[a,*], Huijuan Liu[a], Ping Peng[d]

[a] Key Laboratory of Drinking Water Science and Technology, Research Center for Eco-Environmental Sciences, Chinese Academy of Sciences, Beijing 100085, China
[b] University of Chinese Academy of Sciences, Beijing 100049, China
[c] Brook Byers Institute for Sustainable Systems and School of Civil and Environmental Engineering, Georgia Institute of Technology, 828 West Peachtree Street, Atlanta, GA 30332, United States
[d] School of Materials Science and Engineering, Hunan University, Hunan 410082, China

GRAPHICAL ABSTRACT

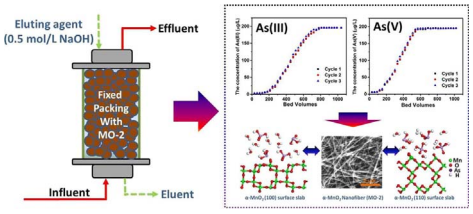

ARTICLE INFO

Keywords:
Arsenic
Adsorption
α-MnO_2
(1 1 0)
(1 0 0)

ABSTRACT

The adsorption behavior of arsenic (As) on specific crystalline phases of manganese dioxide (MnO_2) remains unclear. In this study, we evaluated the ability of α-MnO_2 nanofibers (MO-2) to remove both arsenite (As(III)) and arsenate (As(V)), using experimental and computational methods. The maximum adsorption capacity values of As(III) and As(V) on MO-2 were 117.72 and 60.19 mg/g, respectively, which is higher than values reported for α-MnO_2, β-MnO_2 and γ-MnO_2. In particular, because MO-2 has much higher adsorption capacity for As(III) than As(V), it can be effectively applied in removal of As(III) from groundwater, and a pre-oxidation process is not required. Fixed-bed tests showed that about 800 mL As(III)- or 480 mL As(V)-contaminated water could be treated before breakthrough, and MO-2 can be effectively regenerated using only 12 mL of eluent. This means we can concentrate the As(III) and As(V) by factors of 66.6 and 40.0, respectively. According to density functional theory (DFT) calculations, As(III) and As(V) form stable complexes on (1 0 0) and (1 1 0) of α-MnO_2. Moreover, the surface complexes of As(III) and As(V) on (1 0 0) are more stable than (1 1 0). Electron transfer from As(III) on (1 0 0) is greater than (1 1 0). These phenomenon are may due to the fact that (1 0 0) has lower surface energy than (1 1 0). Partial density of state (PDOS) analysis further confirmed that As(III, V) are chemisorbed on MO-2, which agreed with the Dubinin-Radushkevich model.

1. Introduction

Heavy metals contamination in water, especially arsenic (As), has become a worldwide problem in recent decades. Arsenic can cause many human ailments and diseases, including kidney disease, reproductive failure, central nervous system, liver and brain damage [1]. Drinking water is the major exposure pathway for As that can affect humans, and causes serious health risk in many parts of the world, such

* Corresponding author.
E-mail address: czhu@rcees.ac.cn (C. Hu).

http://dx.doi.org/10.1016/j.cej.2017.08.123
Received 3 July 2017; Received in revised form 28 August 2017; Accepted 28 August 2017
Available online 06 September 2017
1385-8947/

as Argentina, Bangladesh, Chile, China, Hungary, India (West Bengal), Mexico, Romania, Taiwan, Vietnam, many parts of the USA, Nepal, Myanmar and Cambodia [2–5]. As a result, the United States Environmental Protection Agency (USEPA) has decreased the maximum contaminant level (MCL) of As from 50 μg/L to 10 μg/L in drinking water, because of the severe negative impact of As on human health [6].

Nowadays, adsorption has been recognized as the most appropriate and effective technique for As removal from water, due to its high efficiency, simplicity of operation, and low cost [7–9]. Meanwhile, adsorption technique is especially useful for treating lower concentrations of As and has commonly been suggested as a polishing step for drinking water purifications [10,11]. Many adsorbents have been synthesized and proposed for As removal, including metal oxide/activated carbon [12,13], biochar [14], biomass sorbents [15], and organic polymers [16]. However, the adsorption capacities of the reported adsorbents were relatively low, and the understanding of intrinsic adsorption mechanism is still very limited. In natural water, arsenic mainly exists as the arsenite (As(III)) and arsenate (As(V)). As(III) has higher mobility and toxicity than As(V), and is commonly present in ground water [17]. Many studies have only focused on the removal of one As species (i.e. As(III) or As(V)) from water via adsorption [18–22]. Meanwhile, many reported adsorbents exhibit higher adsorption capacity for As(V) than As(III), and conventional iron-based adsorption technologies require the oxidation of As(III) to As(V) because the adsorption capacity for As (III) is much lower than for As(V) [23–27]. Accordingly, we have focused on the synthesis of a highly effective adsorbent to simultaneously remove As(III) and As(V) from aqueous solution, especially for As(III). Combining with the systematically adsorption mechanism analysis of As on the adsorbent.

Manganese (Mn) is one of the most abundant and widespread elements on earth, and it is non-toxic and inexpensive. Moreover, Mn-oxides have a strong affinity toward metal ions due to their large specific surface areas, typically in the range of 50–300 m^2/g [28,29]. Among Mn-oxide adsorbents, manganese dioxide (MnO_2) is one of the most stable Mn-oxides under ambient conditions. In recent decades, there has been great interest in using MnO_2 as an adsorbent for the removal of various heavy metals from aquatic systems, including Cr (VI), Pb(II), Cd(II), and Zn(II) [30–33]. In addition, α-MnO_2 has shown great advantages as a catalyst in phenol degradation [34] and carbon monoxide oxidation [35]. It has also been shown that it can be used to synthesize highly efficient supercapacitor electrodes [36]. Nevertheless, to the best of our knowledge, systematic studies of the removal of As (III) and As(V) from water using α-MnO_2 are still very limited.

Quantum chemical calculations, such as density functional theory (DFT), have been applied to investigate geochemical processes, including interactions between adsorbents and adsorbates [37–41], especially between As and other metal oxides or metal hydroxyl compounds. By using DFT calculations, Yan et al. have determined adsorption surface complexes of As(V) on the rutile (1 1 0) surface, and confirmed As(V) bound in an inner-sphere fashion with the edge/corner-sharing tridentate (ECT) complex is the most favorable adsorption configuration [42]. Meanwhile, He et al. have identified that the adsorption of As(V) on TiO_2 surfaces involved not only chemical bond but also H-bond, especially at low pH. And both monodentate and bidentate complexes were formed between As(V) and TiO_2 surfaces [43]. Oliveira et al. have proposed mechanisms for As(III) on gibbsite-γ-Al$(OH)_3$ using DFT calculations, which confirmed that As(III) is not adsorbed via an acid/base, but by a non-dissociative mechanism in which O–H bonds are not being broken [44]. While the adsorption surface complexes between As and Mn-oxides and its intrinsic mechanisms are seldom studied. Only Zhu et al. have investigated the interaction between As(III, V) and Mn-oxides by using DFT calculations [45]; and Hou et al. have elucidated the effect of oxygen vacancy defects on the oxidation of As(III) to As(V) on cryptomelane-type manganese oxides using both experimental and computational results (DFT calculations) [46]. To the best of our knowledge, the adsorption mechanism of As(III, V) on different facets of typical MnO_2 (i.e. α-MnO_2) have not been extensively studied via DFT calculations.

In this study, the adsorption behavior of As(III, V) onto α-MnO_2 nanofibers (MO-2) was comprehensively studied in both varies experimental methods and theoretical calculations (i.e. DFT calculations). MO-2 has shown great performance on As removal, and the adsorption capacity on As(III) and As(V) were 117.72 and 60.19 mg/g, respectively. Noteworthy, the adsorption ability of MO-2 on As(III) is nearly two times higher than As(V), which can be effectively applied in removal of As(III) from groundwater, and a pre-oxidation process is not required. Meanwhile, the adsorption mechanisms of As(III, V) on two different facets in α-MnO_2, including (1 1 0) and (1 0 0), were further identified. The present work provides an efficient Mn oxide-related adsorbent which applicable for As removal from aqueous solutions.

2. Materials and methods

2.1. Chemicals and materials

All chemicals were analytical grade and used without further purification. The stock solutions of As(III) and As(V) with the concentration of 500 mg/L were prepared in deionized (DI) water using sodium arsenate ($Na_2HAsO_4{\cdot}12H_2O$) and sodium arsenite ($NaAsO_2$). Graphite powder, ethanol, potassium hydroxide (KOH), and potassium permanganate ($KMnO_4$) were used for the synthesis of α-MnO_2 nanofibers. The α-MnO_2 nanofibers were prepared by a hydrothermal method, and the synthesis procedure was detailed in the Supporting Information, Section 1.

2.2. Characterization

The crystalline phase samples were analyzed using X-ray diffraction (XRD, Rigaku UltimaIV) using graphite monochromatized Cu-Ka (λ = 1.5406 Å) radiation. X-ray photoelectron spectroscopy (XPS) measurements were carried out with a VG Escalab 250 spectrometer that was equipped with an Al anode (Al-*K*α = 1486.7 eV). The Brunauer-Emmett-Teller (BET) specific surface areas and porosity were determined by using nitrogen-sorption isotherms via a Micrometritics ASAP 2010 analyzer.

2.3. Adsorption experiments

As(III) and As(V) solutions (50 mL) with initial concentrations ranging from 10 to 270 mg/L were prepared by diluting the corresponding stock solutions with DI water. Batch experiments were used to determine the adsorption isotherms of As(III) and As(V). The adsorption isotherms for As(III) and As(V) at different temperatures (20, 30, 40 °C) were analyzed. The dosage of adsorbent for all the experiments was 0.5 g/L. The adsorption capacity (q_e) for As was calculated according to the following Eq. (1):

$$q_e = \frac{V(C_0 - C_e)}{m} \quad (1)$$

where q_e (mg/g) is the equilibrium adsorption capacity; C_0 and C_e (mg/L) are the initial and equilibrium concentrations of the adsorbate in solution, respectively; V is the volume (mL) of As solution; m is the mass (mg) of adsorbent used in the experiment. All the adsorption modeling equations can be found in Supporting Information, Section 2.

Fixed-bed column sorption experiments were carried out at ambient temperature using as-prepared MO-2 packed in fixed-bed columns. The influent concentration was 200 μg/L for both As(III) and As(V). The fixed bed was fed in down-flow mode using a peristaltic pump. 0.5 mol/L sodium hydroxide (NaOH) solution was used as the eluting agent for desorption. Then MO-2 was washed using DI water for the repeat use. The column parameters are summarized in Table S1.

2.4. Effects of pH

In order to analyze the effect of pH on As removal, the pH values varied from 3.0 to 13.0 were adjusted using 0.1 mol/L HCl or 0.1 mol/L NaOH. The concentration of As(III) and As(V) were 100 mg/L and 90 mg/L, respectively. All the suspensions for the isotherm tests were sealed and stirred in a thermostatic oscillator at 240 rpm for 24 h. After the adsorption, all the suspensions were filtered through 0.45 μm cellulose acetate membranes and analyzed.

2.5. Regeneration and reuse

In the experiment, 100 mg of MO-2 was added into 200 mL of 170 mg/L and 180 mg/L As(III) and As(V) solution at pH 6.0, and the mixture was stirred in a thermostatic oscillator at 240 rpm for 24 h. After adsorption, the MO-2 was removed from the solution and rinsed with water. For regeneration, the spent MO-2 was immersed in 0.5 mol/L NaOH solution and stirred for 2 h in a thermostatic oscillator. The above procedure was repeated until there was no detection of As in the eluent. Then MO-2 was removed from the solution and washed with DI water. The MO-2 was dried at 50 °C before being reused in the next cycle. The adsorption-regeneration cycles were repeated for 5 times with the As adsorption capacity monitored.

2.6. Impact of additional anions in solution

The impact of competing anions on the removal of As(III) and As(V) was evaluated by adding NaF, NaCl, Na_2SO_4, $NaNO_3$, $NaHCO_3$ and/or $Na_3PO_4{\cdot}12H_2O$. The concentration of the competing ions was 2.5 mM (which corresponds to 48.20, 87.65, 237.54, 162.32, 160.03, 218.54 mg/L, respectively). The initial concentration of As(III) or As(V) was 180 mg/L. The initial pH value of the solution was adjusted to 6.0 with 0.1 mol/L HCl or NaOH. The adsorption experiment was conducted using 20 mL solution and the dosage of the adsorbent was 0.5 g/L. After adding the adsorbent, the mixture was shaken at 20 °C for 12 h. The initial and equilibrium concentrations of As in this study were determined using an 8220 atomic fluorescence spectrophotometer. All the data points are carried out with the triplicate mean value.

2.7. Computational methods

All the calculations were performed with the Castep package using Material Studio 7.0. For the plane wave calculations, a cutoff energy of 450 eV was used. The exchange-correlation interaction was treated within the generalized gradient approximation (GGA) using the Perdew, Burke and Enzerhof (PBE) functional parameterization. In order to further improve the accuracy of the band gap calculation of (1 1 0) and (1 0 0) surface slabs, an on-site Coulomb potential (DFT + U) correction was applied to the 3d electron structure of Mn atoms [47–49]. The optimized Hubbard U = 1.6 eV was chosen in this study, which is consistent with previous studies [50,51]. The convergence criteria of SCF and energy tolerances were set as 5.0×10^{-5} and 1.0×10^{-5} eV/atom, respectively. A Monkhorst-Pack scheme with a $2 \times 1 \times 1$ k-point grid was employed as well.

The bulk unit cell of α-MnO_2 was first geometry-optimized, resulting in lattice parameters a = b = 9.898 Å and c = 2.924 Å, which are consistent with the experimental data (a = b = 9.750 Å and c = 2.861 Å). The accuracy of the results validated the applicability of the Castep package to calculate our α-MnO_2 slab structures. Both (1 1 0) and (1 0 0) surface slabs were cleaved from the optimized bulk structure of α-MnO_2. Fourteen layers of (1 1 0) atoms and seven layers of (1 0 0) atoms were extracted, respectively, and then a 2×3 supercell was built. Periodic boundary conditions were applied in all three dimensions with a vacuum region of 15 Å along the z-axis. In order to keep the computational cost relatively low, the atoms in the top seven layers of the (1 1 0) slab were relaxed, whereas the atoms in the bottom seven layers were constrained during the optimization. For the (1 0 0) slab calculations, the atoms in the top four layers of the slab were relaxed, whereas the atoms in the bottom three layers were constrained. Optimized H_3AsO_3 and H_2AsO_4 molecules were added to the optimized (1 1 0) and (1 0 0) surface slabs to build the initial interfacial complex. To further simulate the adsorption of H_3AsO_3 and H_2AsO_4 on the (1 1 0) and (1 0 0) surfaces of α-MnO_2 in water, four water molecules were added to the optimized (1 1 0) and (1 0 0) surface slabs, along with H_3AsO_3 and H_2AsO_4, respectively [42].

The adsorption energy (E_{ad}) for As adsorbed on optimized (1 1 0) and (1 0 0) surface slabs of α-MnO_2 is calculated as Eq. (2):

$$E_{ad} = E_{As+surf} - (E_{surf} + E_{As}) \quad (2)$$

where $E_{As+surf}$ is the total energy, E_{surf} is the energy of the surface; E_{As} is the energy of an isolated H_3AsO_3 or H_2AsO_4 molecule [52–54].

The net charge of atoms during As adsorption was calculated as Eq. (3):

$$\text{Net Charge} = \text{Mulliken Charge}_{after} - \text{Mulliken Charge}_{before} \quad (3)$$

where Mulliken charge_{after} is the charge of atoms after As was adsorbed and Mulliken charge_{before} is the charge of atoms before adsorption. Note that a positive value for the net charge suggests a loss of electrons [55].

3. Results and discussions

3.1. Adsorption isotherms and kinetics

α-MnO_2 (MO-2) was characterized in our previous work, and we have confirmed that this adsorbent was α-$MnO_2$with compact nanofiber morphology [56]. And the pore volume and average pore size of MO-2 are further determined, which is 0.4027 cm^3/g and 20.30 nm, respectively (See Fig. S1, Supporting Information (SI)). The adsorption isotherms of the As(III) and As(V) species on MO-2 at different temperatures are shown in Fig. 1a and b. The adsorption curves suggest that the uptake of As(III) and As(V) decreases as the temperature increases. Langmuir and Freundlich isotherm models were fit to the experimental data. The correlation coefficient (R^2) of the Langmuir model is higher than that of the Freundlich model for both As(III) and As(V) (Table S2, SI). Consequently, the Langmuir model is more suitable to describe the isotherm data. The Langmuir model assumes that the adsorption site energy is the same for all surface sites and does not depend on degree of coverage [57]. This suggests that the largest capacity corresponds to a monolayer, and the surface sites are homogeneous. Moreover, the maximum adsorption capacity of As(III) on MO-2 is much higher than that of As(V), which is 117.72 and 60.19 mg/g, respectively, at 20 °C. Accordingly, As(III) has higher affinity than As(V) toward MO-2, which is confirmed by the larger k_L values, as presented in Table S2.

As comparison, other different crystalline phases of MnO_2 were synthesized, including α-MnO_2, β-MnO_2, and γ-MnO_2 [34]. The crystalline phases of as-prepared MnO_2 were further characterized and confirmed using XRD (Fig. S2). The Langmuir isotherm model is suitable to describe the behavior of As(III, V) on α-MnO_2, β-MnO_2, and γ-MnO_2 (Fig. S3 and Table S3, SI). The maximum adsorption capacity of As(III) on α-MnO_2, β-MnO_2, and γ-MnO_2 is 32.30, 40.63 and 64.84 mg/g, respectively. In contrast, the maximum adsorption capacity of As(V) on α-MnO_2, β-MnO_2, and γ-MnO_2 is 44.56, 29.37 and 57.83 mg/g, respectively. Therefore, MO-2 has higher adsorption capacity on As(III, V) than α-MnO_2, β-MnO_2, and γ-MnO_2, especially on As(III). The higher adsorption capacity of As(III, V) on MO-2 as compared to reported α-MnO_2 could mainly due to the differences in proportions of exposed facets according to the XRD patterns. The main facet of MO-2 is (3 1 0), while it is (2 1 1) for the literature-reported α-MnO_2 (see Fig. S2a and S2b, SI). Meanwhile, the (4 0 0) facet, which belongs to the most stable (1 0 0) facet group in α-MnO_2, is more evident in MO-2 than the reported α-MnO_2, which could be another reason for the observed behavior [49]. Furthermore, the BET surface areas of reported α-MnO_2, β-

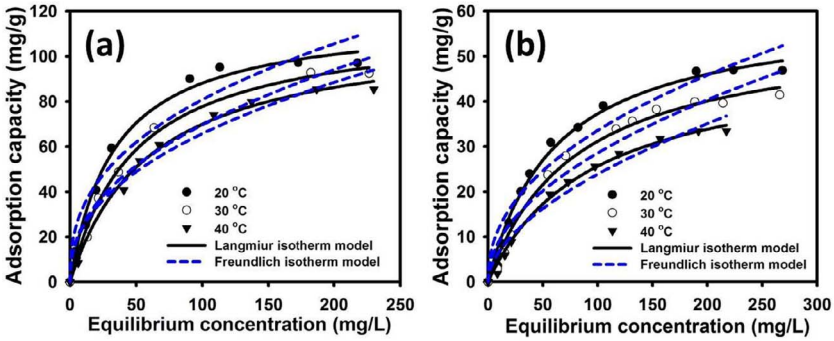

Fig. 1. Adsorption isotherm at different temperatures for (a) As(III) and (b) As(V) on MO-2. Initial As(III) and As(V) concentration 10–270 mg/L; adsorbent dose 0.5 g/L; solution volume 50 mL; and pH 6.0.

MnO_2, and γ-MnO_2 are 148, 194 and 83 m^2/g, respectively. The BET surface area of MO-2 is 144 m^2/g, which is smaller than reported α-MnO_2 and β-MnO_2. However, the adsorption capacities of MO-2 for As (III, V) are much higher than the literature-reported α-MnO_2 and β-MnO_2. This could mainly due to the morphologies of these adsorbents are distinctly different, which suggests that the morphology of the adsorbent may contribute to its higher adsorption capacity. In addition, the adsorption capacity of MO-2 is also higher than many other reported literatures (Table S4, SI).

Meanwhile, q_m and k_L are decreased with increasing temperature, which indicates an exothermic adsorption process. This can be further confirmed by thermodynamic analysis using Eqs. (4) and (5):

$$\Delta G^o = -RT\ln k_L \tag{4}$$

$$\ln k_L = \frac{\Delta S^o}{R} - \frac{\Delta H^o}{RT} \tag{5}$$

where R is the universal gas law constant (8.314 × 10^{-3} kJ/mol·K); T is the absolute temperature (K); and k_L is the Langmuir adsorption equilibrium constant (L/mg). ΔH° and ΔS° can be determined according to Eq. (5). The values of ΔH° and ΔS° were calculated from Figs. S4a and S4b, depicted in Table S5, in Supporting Information.

All the values of ΔG° are negative, which means that the adsorption process of As(III, V) onto MO-2 is favorable (see Table S5, SI). For As (III), ΔG° are −8.26, −7.63 and −7.29 kJ/mol at 20, 30, and 40 °C, respectively; and ΔH° and ΔS° are −22.54 kJ/mol and −0.049 kJ/mol·K, respectively. For As(V), the ΔG° values are −6.80, −6.37 and −6.14 kJ/mol at 20, 30, and 40 °C, respectively; and ΔH° and ΔS° are −16.42 kJ/mol and −0.033 kJ/mol·K. ΔG° increases with increasing temperature, indicating that the adsorption process is favorable; and lower temperature is more favorable for both As(III, V) adsorption. The negative value of ΔH° suggests an exothermic reaction for the adsorption process for both As(III, V), and the negative ΔS° values reveal the decreasing randomness at the adsorbent/adsorbate interface during the adsorption processes [58,59].

Furthermore, we used the Dubinin-Radushkevich model to determine the nature of adsorption process (i.e. chemical or physical) [60]. The linear equation of the D-R isotherm is expressed as Eq. (6):

$$\ln q_e' = \ln q_m' - \beta\varepsilon^2 \tag{6}$$

where q_e' is the amount of metal ions adsorbed per unit weight of the adsorbent (mol/g), q_m' is the maximum adsorption capacity (mol/g), β is the activity coefficient related to the mean free energy of adsorption (mol^2/kJ^2), and ε is the Polanyi potential ($\varepsilon = RT\ln(1 + 1/C_e)$). The values of q_m' and β were calculated from Fig. S4c and S4d, depicted in Table S6, in Supporting Information.

The mean free energy of adsorption (E; kJ/mol) is expressed as Eq. (7):

$$E = \frac{1}{\sqrt{2\beta}} \tag{7}$$

A value of E between 8 and 16 kJ/mol indicates that the adsorption process is chemisorption. We determined E values of 9.46 and 8.17 kJ/mol for As(III) and As(V) adsorption, respectively. Thus, both As(III) and As(V) are chemisorbed on the surface of MO-2.

Adsorption kinetic parameters are indispensable when designing adsorption units, optimizing operation conditions and controlling the recycle time of a fixed bed experiment. It can be seen that adsorption process is rapid during the first 30 min, slowed down thereafter, and finally reached equilibrium (see Fig. S5). In order to further analyze the rate-controlling step in the adsorption mechanism, the kinetic data were fit with pseudo-first and pseudo-second order kinetic models.

The kinetic parameters calculated from the pseudo-first and pseudo-second order kinetic models were detailed in Table S7. In general, slightly higher correlation coefficient was achieved by pseudo-second order kinetic model on both As(III, V) adsorption kinetic process. Based on pseudo-second order kinetic model is based on the assumption that rate-limiting step might be chemisorption or exchange of electrons between the adsorbent and adsorbate [61,62]. This suggests that both As(III, V) are chemisorbed on the surface of MO-2.

The mass transfer model was applied to further analyze As(III, V) kinetic data (Fig.2a). The details of the mass transfer mathematical derivation equations were shown in Section 3 in Supporting Information. The mass balance equations are:

$$-\frac{dC}{dt} = k_f \times a(C - C_s) \tag{8}$$

$$C = b\exp[-ht] + C_0 - b \tag{9}$$

where C is the concentration of As (mg/L) in the bulk solution at time t, C_s is the concentration of As at the interface (mg/L), h and b are fitting parameters, and k_f is the mass transfer coefficient (cm/s).

The calculated k_f value are 1.29 × 10^{-4} cm/s (R^2 = 0.9969) and 3.07 × 10^{-5} cm/s (R^2 = 0.9942) for As(III) and As(V), respectively. It is evident that the k_f of As(III) is higher than that of As(V). This phenomenon suggests that the adsorption kinetics of As (III, V) is controlled by mass transfer and that the surface reaction rate is very fast.

Meanwhile, breakthrough curves for As(III, V) from the fixed-bed experiment are also indispensable in facility design and field pilot studies [63]. The column parameters and flow-through experiment operation schematic flowchart were summarized in Table S1 and Fig. S6, respectively. As shown in Fig. 2b and c, the treatment volumes of MO-2 reach 200 bed volumes (BV) (800 mL) for As(III) and 120 BV (480 mL) for As(V), respectively, before 10 μg/L breakthrough line of As, which is the limit for As in drinking water. The breakthrough curves for As(III) and As(V) after three cycles were nearly perfectly superimposed, confirming that the MO-2 adsorbent can be regenerated and reused without adsorption capacity loss. Furthermore, Fig. 2d illustrates that the adsorbed As(III) and As(V) can be entirely eluted with only 3 BV (12 mL) of 0.5 mol/L NaOH solution. In other words, 800 mL As(III) or 480 mL As(V) contaminated water can be effectively treated and produce only 12 mL of eluent. This means the As(III) and As(V) can be concentrated by factors of 66.6 and 40.0, respectively. As a result, the fixed-bed column experiment confirms that MO-2 is potentially

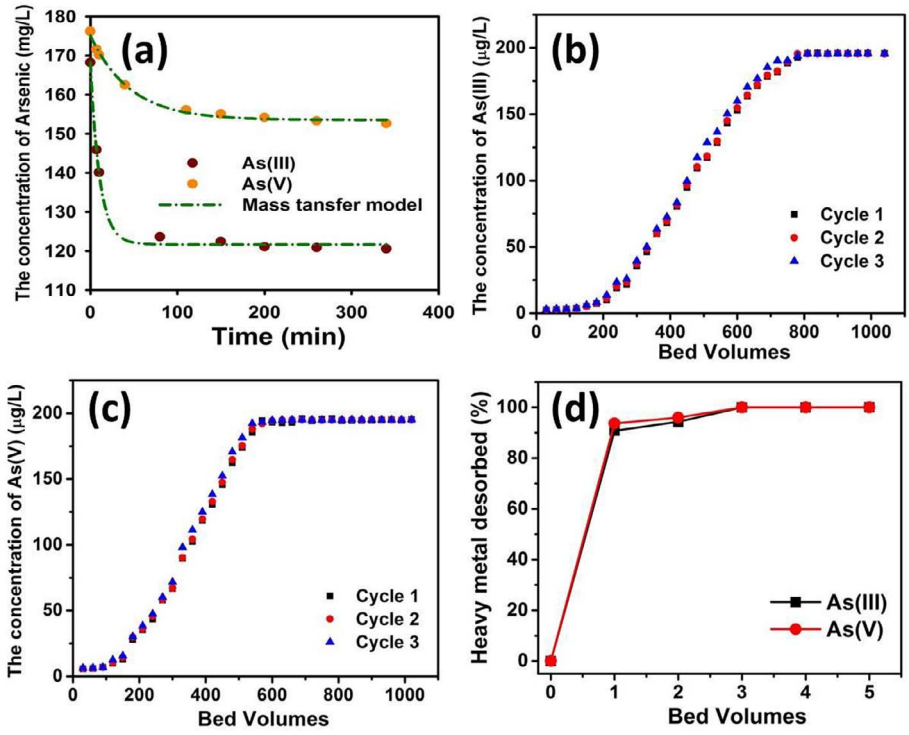

Fig. 2. (a) Adsorption kinetics for As(III) and As(V) adsorption on MO-2 simulated using the mass transfer model (Initial concentrations of As(III) and As(V) 170 mg/L and 180 mg/L, respectively; adsorbent dose 0.5 g/L; solution volume 200 mL), (b) breakthrough curves of As(III) sorption from feeding solution, (c) breakthrough curves of As(V) sorption from feeding solution, and (d) dynamic desorption history of As(III) and As(V). Note: 1 BV is 4.0 mL, and all experiments were conducted at 20 °C, pH 6.0.

applicable for highly efficient removal of As from contaminated water.

3.2. Effect of pH on adsorption

It is known that pH value has an evident impact on the adsorbent performance for As. In this study, the impacts of pH values from 3.0 to 13.0 were evaluated. Fig. S7 displays the adsorption capacity of MO-2 for As(III, V) as a function of pH. The highest adsorption capacity of MO-2 was achieved at pH 5.0, which account for 86.09 and 34.93 mg/g for As(III) and As(V), respectively. And the adsorption capacity decreased when pH higher than 5.0. The reason that the adsorption capacity of MO-2 toward As(III, V) varies is attributed to changes in (1) the degree of ionization of As species with pH, and (2) the zeta potential of the adsorbent a function of pH. In our previous study, we determined the zero charge point (pH_{pzc}) of MO-2 is 4.8 [56].

For As(III), the adsorption capacity decreased after pH 5.0, and dramatically decreased when pH increase from 8.0 to 10.0. As(III) exists as H_3AsO_3 with pH values from 0 to 8.0, but when pH is greater than 8.0, the predominant As(III) species become negatively charged (i.e. $H_2AsO_3^-$, $HAsO_3^{2-}$ and AsO_3^{3-}) [6]. As a result, the adsorption capacity of As(III) on MO-2 decreases when pH greater than 8.0. This is mainly due to the surface of MO-2 is negatively charged and As(III) species are negatively charged as well, result in the enhancement of Coulombic repulsion between As(III) and MO-2 surface. For As(V), the adsorption capacity increased as pH increased from 3.0 to 5.0, and then decreased dramatically as pH increased from 5.0 to 7.0. And the adsorption capacity gradually decreased when pH above 7.0. For pH values from 4.0 to 8.0, As(V) exists as $H_2AsO_4^-$ and $HAsO_4^{2-}$; and exists as AsO_4^{3-} when pH greater than 8.0. The MO-2 surface is positively charged when pH below 5.0, and negatively charged thereafter. As a result, when pH values below 5.0, Coulombic attraction exists, and causes an increase in the adsorption capacity of MO-2. For pH values from 5.0 to 13.0, Coulombic repulsion exists, which first leads to a dramatic decrease in the adsorption capacity as the pH increases from 5.0 to 7.0 and then gradual decrease after pH 7.0.

3.3. Regeneration and reuse

The regeneration and recycling behavior of the MO-2 were investigated during five successive reuse cycles to investigate MO-2 performance. The spent MO-2 was recovered by shaking in 0.5 mol/L NaOH solution at 240 rpm for 2 h, followed by centrifugation. The regenerated adsorption capacity of MO-2 is shown in Fig. S8. The capacity of reused MO-2 remained intact for the first two cycles and then slightly dropped after the 5th cycle. After five regeneration cycles, the adsorption capacity of MO-2 for As(III) and As(V) only decreased by 9.5% and 16.1% compared with the first cycle, illustrating that MO-2 can be repeatedly used.

3.4. Effect of competing anions

In contaminated water, arsenic is usually accompanied by other different anions, such as fluoride (F^-), chloride (Cl^-), sulfate (SO_4^{2-}), nitrate (NO_3^-), bicarbonate (HCO_3^-) and phosphate (PO_4^{3-}), which may compete with As for the available active sites on the adsorbent. Even though F^-, Cl^-, SO_4^{2-}, NO_3^-, HCO_3^- and PO_4^{3-} were initially present at 2.5 mmol/L, the As(III, V) adsorption capacity was not significantly reduced, even when PO_4^{3-} was present (see 1). In many other studies, PO_4^{3-} was shown to greatly reduce the adsorbent adsorption capacity on As. This is because the molecular structure of phosphate ion is very similar to that of As [64–67]. Our work confirms the superior advantage of MO-2 as compared to many other adsorbents in the presence of PO_4^{3-}. Meanwhile, MO-2 has also shown great performance on As(III, V) removal even six anions were present simultaneously with initial concentrations as high as 2.5 mmol/L in aqueous solution. The adsorption capacity of MO-2 toward As(III) and As(V) in the mixed six anions solution is 19.53% and 26.17% lower than that in the DI water, respectively (see Fig. S9c and S9d, SI). It confirms that the adsorption performance of MO-2 is still acceptable and relatively high even under severe ambient conditions.

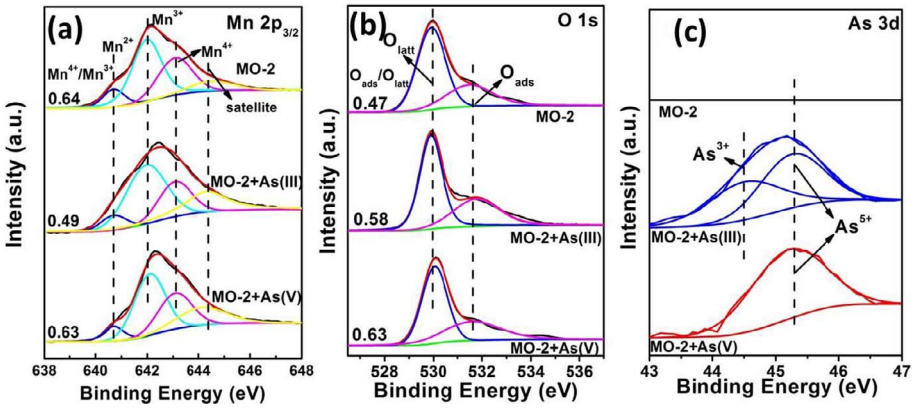

Fig. 3. XPS spectra of (a) Mn $2p_{3/2}$, (b) O 1s and (c) As 3d of different samples. Note: MO-2 represents pristine MO-2; MO-2 + As(III) represents MO-2 after As(III) adsorption; MO-2 + As(V) represents MO-2 after As(V) adsorption; O_{latt} is lattice oxygen; O_{ads} is surface adsorbed oxygen.

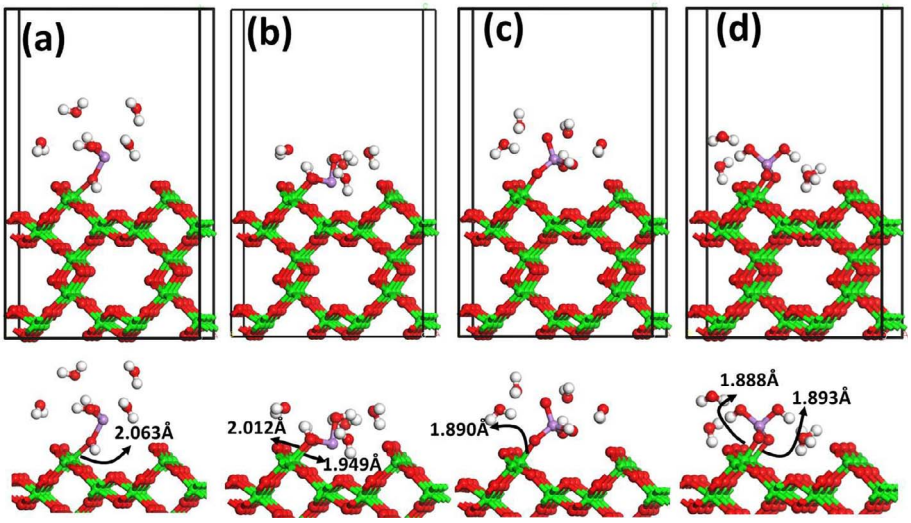

Fig. 4. Optimized As(III) (a) monodentate (A-1) and (b) bidentate (A-2) complex on (1 1 0); Optimized As(V) (a) monodentate (B-1) and (b) bidentate (B-2) complex on (1 1 0). Arsenic atoms are purple, oxygen atoms are red, manganese atoms are green, and hydrogen atoms are white.

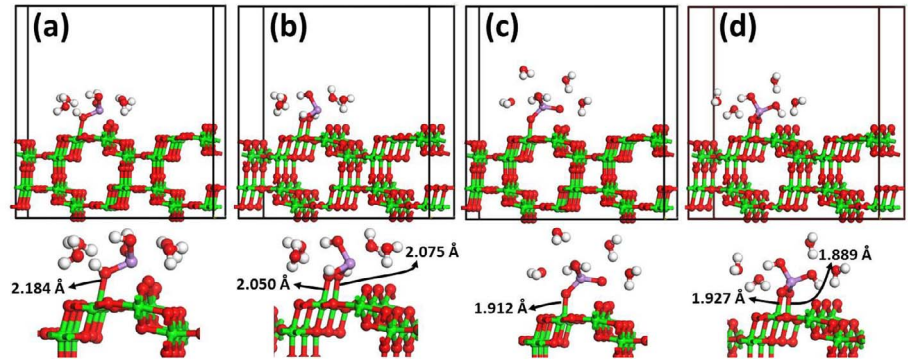

Fig. 5. Optimized As(III) (a) monodentate (C-1) and (b) bidentate (C-2) complex on (1 0 0); Optimized As(V) (a) monodentate (D-1) and (b) bidentate (D-2) complex on (1 0 0). Arsenic atoms are purple, oxygen atoms are red, manganese atoms are green, and hydrogen atoms are white.

3.5. XPS analysis

The surface element composition, metal oxidation states, and adsorbed species of solid material can be detected using XPS measurements. Fig. 3 shows Mn $2p_{3/2}$, O 1s and As 3d XPS spectra of the three samples with different treatments. In Fig. 3a, it can be seen that the asymmetrical Mn $2p_{3/2}$ XPS spectrum of each sample can be deconvoluted into four components at binding energy (BE) = 640.7, 642.1, 643.1, and 644.2 eV, which can be assigned to the surface Mn^{2+}, Mn^{3+}, Mn^{4+} species and a satellite peak for the Mn^{3+} species, respectively [68–70]. The Mn^{4+}/Mn^{3+} molar ratio of pristine MO-2 (0.64) is evidently higher than that of MO-2 after As(III) adsorption (0.49). This phenomenon is mainly due to the redox reaction that takes place during As(III) adsorption. The Mn^{4+}/Mn^{3+} molar ratio of MO-2 after As(V) adsorption is identical (0.63), indicating no redox reaction occurred. As shown in Fig. 3b, the XPS spectrum of O 1s can be deconvoluted into two individual components at BE = 529.9 and 531.5, respectively, which corresponds to the lattice oxygen (O_{latt}) and surface adsorbed oxygen (O_{ads}). The O_{ads}/O_{latt} ratio of pristine MO-2 is 0.47, and determined to be 0.58 and 0.63 after As(III) and As(V) adsorption. The results further confirm that both As(III, V) are adsorbed on the MO-2 surface. The difference of O_{ads}/O_{latt} ratio after As(III) and As(V) adsorption is mainly due to the different existence species of As (for As (III), this is H_3AsO_3; for As(V), $H_2AsO_4^-$). Meanwhile, the BE values of As(III) and As(V) at the As 3d core level are 44.3–44.5 and 45.2–45.6 eV, respectively [71]. As shown in Fig. 3c, for the As(III) adsorbed on

MO-2, individual As(III) and As(V) signals are present at 44.5 and 45.3 eV, respectively, and 53.48% of As(III) is oxidized to As(V). By contrast, only As(V) is observed at 45.2 eV in the sample of MO-2 with As(V), showing that no oxidation reaction takes place during the adsorption process of As(V) on the surface of MO-2.

3.6. DFT calculations

As reported by Tompsett et al. [49], (1 1 0) and (1 0 0) are the two most stable facets in α-MnO_2, with surface energies lower than 1 J/m^2. The surface energy of (1 0 0) is even lower than (1 1 0). Hence, (1 1 0) and (1 0 0) facets were used to identify and compare the As(III, V) adsorption behavior. The optimized (1 1 0) and (1 0 0) surface slabs are shown in Fig. S10.

As shown in Fig. 4a, As(III) is monodentate on the (1 1 0), with a single Mn-O bond (2.063 Å). The adsorption energy (E_{ad}) of this complex is determined to be −0.97 eV. Meanwhile, As(III) can also form bidentate complex on (1 1 0), with two Mn-O bonds (2.012 Å and 1.949 Å) (Fig. 4b). The E_{ad} of bidentate complex is −2.16 eV, which is lower than monodentate complex, which indicates that bidentate complex is more stable than monodentate complex. The net charge analysis revealed that As(III) lost 0.10 *e* and 0.04 *e*, and the bonded O atom also lost 0.1 *e* and 0.2 *e* in monodentate and bidentate complexes, respectively. Under this circumstance, the bond strength of As-O evidently weakened, which suggested the As(III) is less stable after adsorption and easily to be oxidized. Similar adsorption behavior is observed on As(V) adsorption on (1 1 0). For monodentate complex, one Mn-O bond (1.890 Å) is formed with E_{ad} = −1.03 eV (Fig. 4c); for bidentate complex, two Mn-O bonds (1.888 Å and 1.893 Å) are formed with E_{ad} = −2.68 eV (Fig. 4d). By analyzing the As(V) species, the related atoms (i.e. O, Mn), As-O bond strength, and the net charge remain nearly unchanged after adsorption, which suggests that no redox reaction occurs. The details of net charge calculations and adsorption energy calculations of As(III) and As(V) on (1 1 0) are summarized in Tables S8 and S9, respectively. The partial density of states (PDOS) of As(III, V) complexes on (1 1 0) was further identified (Figs. S11 and S12). The two bonding peaks in the valence band (VB) (labeled as I and II) shift to lower energy after adsorption, which indicates that stable adsorption complexes were formed. Meanwhile, the antibonding peak of As(III, V) in the conduction band (CB) (labeled as III) shows a shift to lower energy, which indicates that As(III, V) were chemisorbed on the (1 1 0) surface. Moreover, the PDOS of Mn at Fermi level decreases after As(III, V) adsorption on the surface slab (labeled as IV), which reveals that the activity of Mn is reduced but its stability is increased. This phenomenon further suggests that a chemical reaction takes place between Mn and As. The antibonding peak of Mn in the CB (labeled as V) shifts to lower energy as well, which further demonstrates that the As (III, V) are chemisorbed on (1 1 0).

For comparison, the adsorption behavior of As(III) and As(V) on (1 0 0) were also investigated. As shown in Fig. 5, As(III) and As(V) can form monodentate and bidentate complex on (1 0 0). In Fig. 5a, As(III) is monodentate on (1 0 0) with one Mn-O bond (2.184 Å), and E_{ad} is −1.39 eV. As(III) can also bidentate on (1 0 0) and forms two Mn-O bonds (2.050 Å and 2.075 Å) (Fig. 5b) with E_{ad} of −2.34 eV. Comparing the E_{ad} of two complexes, the bidentate complex is more stable than monodentate complex. The net charge analysis reveals that As(III) lost 0.72 *e* and 0.16 *e* in monodentate and bidentate complex, respectively, and the bonded O atom lost 0.13 *e* for both complexes. Evidently, the bond strength of As-O is weakened after adsorption, which indicates that As(III) is less stable and can be easily oxidized. In Fig. 5c, As(V) is monodentate on (1 0 0) and has one Mn-O bond (1.912 Å), and E_{ad} is −1.45 eV. For the bidentate complex, two Mn-O bonds (1.927 Å and 1.889 Å) are formed on the (1 0 0) with E_{ad} of −2.86 eV (Fig. 5d). The related atoms (i.e. O, Mn), As-O bond strength, the net charge remain nearly unchanged after As(V) adsorption, which indicates that no redox reaction occurs. The details of net charge and adsorption energy calculations of As(III) and As(V) on (1 0 0) were summarized in Tables S10 and S11, respectively. The PDOS of As(III, V) on (1 0 0) is similar to (1 1 0) (Figs. S13 and S14). The bonding peaks (labeled as I and II) in VB shift to lower energy after As(III, V) adsorption, demonstrating that stable adsorption complexes are formed. The antibonding peak (labeled as III) in the CB is evidently weakened and shifts to lower energy, which demonstrates that As(III) and As(V) are chemisorbed on the (1 0 0). The PDOS of Mn at the Fermi level (labeled as IV) is decreased after As(III, V) adsorption, which reveals that the activity of Mn is reduced while its stability is increased. This phenomenon further suggests that chemical reaction occurs between Mn and As. Moreover, the antibonding peak of Mn in the CB (labeled as V) undergoes a shift to lower energy as well, and this further confirms that As(III, V) are chemisorbed on the (1 0 0).

Summarizing the adsorption behavior of As(III) and As(V) on (1 1 0) and (1 0 0), the formed complexes of As(III) and As(V) on (1 0 0) are more stable than on (1 1 0). It is also evident that As(III) loses more electrons on (1 0 0) than (1 1 0), which suggests (1 0 0) has greater oxidizing ability than (1 1 0). Because the surface energy of (1 0 0) is lower than (1 1 0), it can be concluded that the lower surface energy facet has stronger oxidizing ability. By combining computational simulations and experimental results, the (1 0 0) is probably the most important facet for α-MnO_2adsorption process. Furthermore, computational results have shown that facet with lower energy can form more stable surface complex with As, and lower valence As is more easily to be oxidized.

4. Conclusion

The findings of this study reveals that MO-2 has excellent adsorption performance toward As(III) and As(V), with the adsorption capacity of 117.72 and 60.19 mg/g, respectively. The performance of MO-2 on As removal is better than reported α-MnO_2, β-MnO_2, and γ-MnO_2. Moreover, the adsorption behavior of As on MO-2 is exothermic, pH-dependent, and has shown superior performance in the presence of high concentration anions (2.5 mmol/L). Furthermore, DFT calculations suggests that both As(III) and As(V) can form stable complexes on both (1 0 0) and (1 1 0), and the adsorption complex on (1 0 0) is more stable than (1 1 0). The variation of net charge is occurred evidently on (1 0 0) than (1 1 0), which identifies (1 0 0) is more functional than (1 1 0). Based on the experimental and theoretical results, it suggests that the MO-2 can be used as an efficient adsorbent for As removal from water.

Acknowledgements

This work was financially supported by the Major Program of the National Natural Science Foundation of China (No. 51290282) and the National Natural Science Foundation of China (Grant No. 51422813 and No. 51378490). The authors appreciate the support from the Brook Byers Institute for Sustainable Systems, Hightower Chair and Georgia Research Alliance at the Georgia Institute of Technology. The views and ideas expressed herein are solely those of the authors and do not represent the ideas of the funding agencies in any form.

Appendix A. Supplementary data

Supplementary data associated with this article can be found, in the online version, at http://dx.doi.org/10.1016/j.cej.2017.08.123.

References

[1] B.V. Tangahu, S.R. Sheikh Abdullah, H. Basri, M. Idris, N. Anuar, M. Mukhlisin, A review on heavy metals (As, Pb, and Hg) uptake by plants through phytoremediation, Int. J. Chem. Eng. 2011 (2011).
[2] Y. Gan, Y. Wang, Y. Duan, Y. Deng, X. Guo, X. Ding, Hydrogeochemistry and arsenic contamination of groundwater in the Jianghan Plain, central China, J. Geochem. Explor. 138 (2014) 81–93.
[3] V.K. Sharma, M. Sohn, Aquatic arsenic: toxicity, speciation, transformations, and

remediation, Environ. Int. 35 (2009) 743–759.
[4] P. Bhattacharya, A.H. Welch, K.G. Stollenwerk, M.J. McLaughlin, J. Bundschuh, G. Panaullah, Arsenic in the environment: biology and chemistry, Sci. Total Environ. 379 (2007) 109–120.
[5] B.K. Mandal, K.T. Suzuki, Arsenic round the world: a review, Talanta 58 (2002) 201–235.
[6] G. Ungureanu, S. Santos, R. Boaventura, C. Botelho, Arsenic and antimony in water and wastewater: Overview of removal techniques with special reference to latest advances in adsorption, J. Environ. Manage. 151 (2015) 326–342.
[7] S. Saha, P. Sarkar, Arsenic remediation from drinking water by synthesized nano-alumina dispersed in chitosan-grafted polyacrylamide, J. Hazard. Mater. 227 (2012) 68–78.
[8] M. Boutonnet, J. Kizling, P. Stenius, G. Maire, The preparation of monodisperse colloidal metal particles from microemulsions, Colloids Surface 5 (1982) 209–225.
[9] M. Pileni, Nanosized particles made in colloidal assemblies, Langmuir 13 (1997) 3266–3276.
[10] A. Genz, A. Kornmüller, M. Jekel, Advanced phosphorus removal from membrane filtrates by adsorption on activated aluminium oxide and granulated ferric hydroxide, Water Res. 38 (2004) 3523–3530.
[11] K. Al-Malah, M.O. Azzam, N.I. Abu-Lail, Olive mills effluent (OME) wastewater post-treatment using activated clay, Sep. Purif. Technol. 20 (2000) 225–234.
[12] S. Zhang, X.-Y. Li, J.P. Chen, Preparation and evaluation of a magnetite-doped activated carbon fiber for enhanced arsenic removal, Carbon 48 (2010) 60–67.
[13] M. Jang, W. Chen, F.S. Cannon, Preloading hydrous ferric oxide into granular activated carbon for arsenic removal, Environ. Sci. Technol. 42 (2008) 3369–3374.
[14] M. Zhang, B. Gao, S. Varnoosfaderani, A. Hebard, Y. Yao, M. Inyang, Preparation and characterization of a novel magnetic biochar for arsenic removal, Bioresource Technol. 130 (2013) 457–462.
[15] M.X. Loukidou, K.A. Matis, A.I. Zouboulis, M. Liakopoulou-Kyriakidou, Removal of As (V) from wastewaters by chemically modified fungal biomass, Water Res. 37 (2003) 4544–4552.
[16] C.M. Iesan, C. Capat, F. Ruta, I. Udrea, Evaluation of a novel hybrid inorganic/organic polymer type material in the Arsenic removal process from drinking water, Water Res. 42 (2008) 4327–4333.
[17] J. Matschullat, Arsenic in the geosphere-a review, Sci. Total Environ. 249 (2000) 297–312.
[18] W.-H. Choi, P.A. Ghorpade, K.-B. Kim, J.-W. Shin, J.-Y. Park, Properties of synthetic monosulfate as a novel material for arsenic removal, J. Hazard. Mater. 227 (2012) 402–409.
[19] J. Mertens, B. Casentini, A. Masion, R. Pöthig, B. Wehrli, G. Furrer, Polyaluminum chloride with high Al_{30} content as removal agent for arsenic-contaminated well water, Water Res. 46 (2012) 53–62.
[20] B. An, Q. Liang, D. Zhao, Removal of arsenic (V) from spent ion exchange brine using a new class of starch-bridged magnetite nanoparticles, Water Res. 45 (2011) 1961–1972.
[21] M.R. Awual, S. Urata, A. Jyo, M. Tamada, A. Katakai, Arsenate removal from water by a weak-base anion exchange fibrous adsorbent, Water Res. 42 (2008) 689–696.
[22] M.R. Awual, M. Shenashen, T. Yaita, H. Shiwaku, A. Jyo, Efficient arsenic (V) removal from water by ligand exchange fibrous adsorbent, Water Res. 46 (2012) 5541–5550.
[23] M. Jiménez-Cedillo, M. Olguín, C. Fall, A. Colín, Adsorption capacity of iron-or iron–manganese-modified zeolite-rich tuffs for As (III) and As (V) water pollutants, Appl. Clay Sci. 54 (2011) 206–216.
[24] M. Aryal, M. Ziagova, M. Liakopoulou-Kyriakides, Study on arsenic biosorption using Fe(III)-treated biomass of Staphylococcus xylosus, Chem. Eng. J. 162 (2010) 178–185.
[25] W.-G. Li, X.-J. Gong, K. Wang, X.-R. Zhang, W.-B. Fan, Adsorption characteristics of arsenic from micro-polluted water by an innovative coal-based mesoporous activated carbon, Bioresource Technol. 165 (2014) 166–173.
[26] C.-H. Liu, Y.-H. Chuang, T.-Y. Chen, Y. Tian, H. Li, M.-K. Wang, W. Zhang, Mechanism of arsenic adsorption on magnetite nanoparticles from water: thermodynamic and spectroscopic studies, Environ. Sci. Technol. 49 (2015) 7726–7734.
[27] A.S.K. Kumar, S.-J. Jiang, Chitosan-functionalized graphene oxide: A novel adsorbent an efficient adsorption of arsenic from aqueous solution, J. Environ. Chem. Eng. 4 (2016) 1698–1713.
[28] Z. Wang, S.-W. Lee, J.G. Catalano, J.S. Lezama-Pacheco, J.R. Bargar, B.M. Tebo, D.E. Giammar, Adsorption of uranium (VI) to manganese oxides: X-ray absorption spectroscopy and surface complexation modeling, Environ. Sci. Technol. 47 (2012) 850–858.
[29] W. Norvell, Inorganic reactions of manganese in soils, manganese in soils and plants, Springer, 1988 pp. 37–58.
[30] M. Gheju, I. Balcu, G. Mosoarca, Removal of Cr (VI) from aqueous solutions by adsorption on MnO_2, J. Hazard. Mater. 310 (2016) 270–277.
[31] S.-G. Wang, W.-X. Gong, X.-W. Liu, Y.-W. Yao, B.-Y. Gao, Q.-Y. Yue, Removal of lead (II) from aqueous solution by adsorption onto manganese oxide-coated carbon nanotubes, Sep. Purif. Technol. 58 (2007) 17–23.
[32] S.S. Tripathy, J.-L. Bersillon, K. Gopal, Adsorption of Cd^{2+} on hydrous manganese dioxide from aqueous solutions, Desalination 194 (2006) 11–21.
[33] X. Li, G. Pan, Y. Qin, T. Hu, Z. Wu, Y. Xie, EXAFS studies on adsorption–desorption reversibility at manganese oxide–water interfaces: II. Reversible adsorption of zinc on δ-MnO_2, J. Colloid Interf. Sci. 271 (2004) 35–40.
[34] E. Saputra, S. Muhammad, H. Sun, H.M. Ang, M. Tade, S. Wang, Different crystallographic one-dimensional MnO_2 nanomaterials and their superior performance in catalytic phenol degradation, Environ. Sci. Technol. 47 (2013) 5882–5887.
[35] S. Liang, F. Teng, G. Bulgan, R. Zong, Y. Zhu, Effect of phase structure of MnO_2 nanorod catalyst on the activity for CO oxidation, J. Phys. Chem. C 112 (2008) 5307–5315.
[36] S. Devaraj, N. Munichandraiah, Electrochemical supercapacitor studies of nanostructured α-MnO_2 synthesized by microemulsion method and the effect of annealing, J. Electrochem. Soc. 154 (2007) A80–A88.
[37] J. Kubicki, K. Kwon, K. Paul, D. Sparks, Surface complex structures modelled with quantum chemical calculations: carbonate, phosphate, sulphate, arsenate and arsenite, Eur. J. Soil Sci. 58 (2007) 932–944.
[38] K.D. Kwon, J.D. Kubicki, Molecular orbital theory study on surface complex structures of phosphates to iron hydroxides: Calculation of vibrational frequencies and adsorption energies, Langmuir 20 (2004) 9249–9254.
[39] A. Ladeira, V. Ciminelli, H. Duarte, M. Alves, A. Ramos, Mechanism of anion retention from EXAFS and density functional calculations: arsenic (V) adsorbed on gibbsite, Geochim. Cosmochim. Ac. 65 (2001) 1211–1217.
[40] K.W. Paul, J.D. Kubicki, D.L. Sparks, Quantum chemical calculations of sulfate adsorption at the Al-and Fe-(hydr) oxide-H_2O interface estimation of Gibbs free energies, Environ. Sci. Technol. 40 (2006) 7717–7724.
[41] D.M. Sherman, S.R. Randall, Surface complexation of arsenic (V) to iron (III)(hydr) oxides: structural mechanism from ab initio molecular geometries and EXAFS spectroscopy, Geochim. Cosmochim. Ac. 67 (2003) 4223–4230.
[42] L. Yan, S. Hu, J. Duan, C. Jing, Insights from arsenate adsorption on rutile (110): grazing-incidence X-ray absorption fine structure spectroscopy and DFT + U study, J. Phys. Chem. A 118 (2014) 4759–4765.
[43] G. He, M. Zhang, G. Pan, Influence of pH on initial concentration effect of arsenate adsorption on TiO_2 surfaces: Thermodynamic, DFT, and EXAFS interpretations, J. Phys. Chem. C 113 (2009) 21679–21686.
[44] A.F. Oliveira, A.C.Q. Ladeira, V.S. Ciminelli, T. Heine, H.A. Duarte, Structural model of arsenic (III) adsorbed on gibbsite based on DFT calculations, J. Mol. Struc-THEOCHEM 762 (2006) 17–23.
[45] M. Zhu, K.W. Paul, J.D. Kubicki, D.L. Sparks, Quantum chemical study of arsenic (III, V) adsorption on Mn-oxides: Implications for arsenic (III) oxidation, Environ. Sci. Technol. 43 (2009) 6655–6661.
[46] J. Hou, J. Luo, Z. Hu, Y. Li, M. Mao, S. Song, Q. Liao, Q. Li, Tremendous effect of oxygen vacancy defects on the oxidation of arsenite to arsenate on cryptomelane-type manganese oxide, Chem. Eng. J. 306 (2016) 597–606.
[47] K.D. Kwon, K. Refson, G. Sposito, Defect-induced photoconductivity in layered manganese oxides: A density functional theory study, Phys. Rev. Lett. 100 (2008) 146601.
[48] D.A. Tompsett, S.C. Parker, M.S. Islam, Rutile (β-) MnO_2 surfaces and vacancy formation for high electrochemical and catalytic performance, J. Am. Chem. Soc. 136 (2014) 1418–1426.
[49] D.A. Tompsett, S.C. Parker, M.S. Islam, Surface properties of α-MnO_2: relevance to catalytic and supercapacitor behaviour, J. Mater. Chem. A 2 (2014) 15509–15518.
[50] Y. Crespo, N. Seriani, Electronic and magnetic properties of α-MnO_2 from ab initio calculations, Phys. Rev. B 88 (2013) 144428.
[51] Y. Crespo, N. Seriani, A lithium peroxide precursor on the α-MnO_2 (100) surface, J. Mater. Chem. A 2 (2014) 16538–16546.
[52] M. Nolan, S.C. Parker, G.W. Watson, The electronic structure of oxygen vacancy defects at the low index surfaces of ceria, Surf. Sci. 595 (2005) 223–232.
[53] Y.-N. Guo, X. Lu, H.-P. Zhang, J. Weng, F. Watari, Y. Leng, DFT study of the adsorption of aspartic acid on pure, N-doped, and Ca-doped rutile (110) surfaces, J. Phys. Chem. C 115 (2011) 18572–18581.
[54] C. Ye, S. Hu, W. Yan, J. Duan, C. Jing, Insights into propranolol adsorption on TiO_2: Spectroscopic and molecular modeling study, J. Phys. Chem. C 117 (2013) 5785–5791.
[55] Z. Liu, L. Ma, A.S. Junaid, NO and NO_2 adsorption on Al_2O_3 and Ga modified Al2O3 surfaces: a density functional theory study, J. Phys. Chem. C 114 (2010) 4445–4450.
[56] J. Luo, C. Hu, X. Meng, J. Crittenden, J. Qu, P. Peng, Antimony removal from aqueous solution using novel α-MnO_2 nanofibers: equilibrium, kinetic, and density functional theory studies, ACS Sustain. Chem. Eng. 5 (2017) 2255–2264.
[57] J.C. Crittenden, R.R. Trussell, D.W. Hand, K.J. Howe, G. Tchobanoglous, MWH's water treatment: principles and design, John Wiley & Sons, 2012.
[58] X.-J. Hu, J.-S. Wang, Y.-G. Liu, X. Li, G.-M. Zeng, Z.-L. Bao, X.-X. Zeng, A.-W. Chen, F. Long, Adsorption of chromium (VI) by ethylenediamine-modified cross-linked magnetic chitosan resin: isotherms, kinetics and thermodynamics, J. Hazard. Mater. 185 (2011) 306–314.
[59] N. Barka, M. Abdennouri, M.E. Makhfouk, Removal of Methylene Blue and Eriochrome Black T from aqueous solutions by biosorption on Scolymus hispanicus L.: Kinetics, equilibrium and thermodynamics, J. Taiwan Inst. Chem. E 42 (2011) 320–326.
[60] M.M. Dubinin, E. Zaverina, L. Radushkevich, Sorption and structure of active carbons. I. Adsorption of organic vapors, Zh. Fiz. Khim. 21 (1947).
[61] Y. Sağ, Y. Aktay, Kinetic studies on sorption of Cr (VI) and Cu (II) ions by chitin, chitosan and Rhizopus arrhizus, Biochem. Eng. J. 12 (2002) 143–153.
[62] S. Azizian, Kinetic models of sorption: a theoretical analysis, J. Colloid Interf. Sci. 276 (2004) 47–52.
[63] L. Yan, Y. Huang, J. Cui, C. Jing, Simultaneous As (III) and Cd removal from copper smelting wastewater using granular TiO_2 columns, Water Res. 68 (2015) 572–579.
[64] Y. Li, J. Wang, Z. Luan, Z. Liang, Arsenic removal from aqueous solution using ferrous based red mud sludge, J. Hazard. Mater. 177 (2010) 131–137.
[65] Z. Gu, J. Fang, B. Deng, Preparation and evaluation of GAC-based iron-containing adsorbents for arsenic removal, Environ. Sci. Technol. 39 (2005) 3833–3843.
[66] A. Ghosh, A.E. Sáez, W. Ela, Effect of pH, competitive anions and NOM on the leaching of arsenic from solid residuals, Sci. Total Environ. 363 (2006) 46–59.
[67] X. Luo, C. Wang, L. Wang, F. Deng, S. Luo, X. Tu, C. Au, Nanocomposites of graphene oxide-hydrated zirconium oxide for simultaneous removal of As(III) and As

(V) from water, Chem. Eng. J. 220 (2013) 98–106.
[68] W. Si, Y. Wang, S. Zhao, F. Hu, J. Li, A facile method for in situ preparation of the MnO_2/$LaMnO_3$ catalyst for the removal of toluene, Environ. Sci. Technol. 50 (2016) 4572–4578.
[69] W. Si, Y. Wang, Y. Peng, J. Li, Selective dissolution of a-site cations in ABO_3 perovskites: a new path to high-performance catalysts, Angew. Chem. 127 (2015) 8065–8068.
[70] W. Si, Y. Wang, Y. Peng, X. Li, K. Li, J. Li, A high-efficiency γ-MnO_2-like catalyst in toluene combustion, Chem. Commun. 51 (2015) 14977–14980.
[71] B. Chen, Z. Zhu, J. Ma, Y. Qiu, J. Chen, Surfactant assisted Ce-Fe mixed oxide decorated multiwalled carbon nanotubes and their arsenic adsorption performance, J. Mater. Chem. A 1 (2013) 11355–11367.